Low-Cost Fabrication of Organic Photovoltaics and Polymer LEDs

Hongseok Youn, Hyunsoo Kim and L. Jay Guo

Abstract Polymer light-emitting diodes (PLEDs) and organic photovoltaics (OPVs) are considered as next generation electronics due to the low-cost, flexibility, and lightweight features. However, there are challenges such as large-area processing technologies, film coating quality, and long-term stability toward scalable and low-cost polymer electronics. This chapter deals with the various scalable processing methods and evaluates the coating performance as well as electrical performances in polymer electronics fabricated by the solution processes. Special attention on coating instability is elaborated in the context of important material components in PLEDs and OPVs. Proper coating techniques can be chosen by considering the thickness requirement of each functional layer with good reproducibility. Additionally, we will evaluate mechanical/optical characteristics of the polymer anode for ITO-free electrodes; and introduce the metal mesh in combination with conductive polymers as the ITO-free transparent electrode for large area applications.

1 Introduction to Roll-Coating Techniques

Polymer electronics have great potential toward large-scale, lightweight, and low-cost devices. Moreover, since polymers can be dissolved in common solvents, polymer electronics can be fabricated using scalable solution processes such as roll-to-roll, inkjet, blade, and spray coating methods. In particular, the polymer solar cells are considered as next generation and sustainable photovoltaic devices. They are attractive as additional power sources for mobile devices and could become ubiquitous in the near future. Moreover, the flexible polymer solar cells could also be applied for building integrated photovoltaics (BIPV) such as walls,

H. Youn · H. Kim · L. J. Guo (✉)
Department of Electrical Engineering and Computer Science, University of Michigan, Ann Arbor, MI 48109, USA
e-mail: guo@umich.edu

Fig. 1 Various future applications of the Polymer Solar Cells with a large-scale and flexible advantages. (The images captured at http://www.solarmer.com/products.html, Copyright © Solarmer Energy Inc)

roofs, and windows as shown in Fig. 1. The manufacturing processes of polymer solar cells are relatively environmentally friendly due to low-emission and waste free features. On the other hand, Polymer LEDs are strong contenders for low-cost and flexible solid-state lighting.

Since the pioneering work of Tang [1], the OLEDs field has witnessed rapid progress. The introduction of triplet phosphorescence materials by Forrest and Thompson [2] has enabled commercialization of small molecule-based OLEDs. In the OPVs area, after the introduction of the bi-layer heterojunction structure by Tang in 1986, the efficient photo-induced charge transfer between conjugated polymer and fullerene in the bulk heterojunction (BHJ) structure was reported by Heeger et al. in 1992 [3]. The power conversion efficiency of the polymer (PBHJ) solar cells has now increased to over 10 % by employing the low band gap polymer [4].

To enable large manufacturing, however, there are few reports on high efficiency OPVs devices fabricated by practical processing. There are some considerations for developing fully printable solar cells. First, the materials should be soluble in common solvents and stable in the air environment. Second, the device structure should be simple and the film thickness should not be too thin considering the variability in film thickness in large area fabrication. If the device structure contains many layers, the limitations and compatibility of solvents for each functional layer should be considered due to the dissolution or intermixing problems with the underlying layers. Thinner layers, e.g., of only a few nanometers thickness, are very challenging to realize uniform film thickness in the large area devices. Third, the cost of the process and that of materials and substrates should not be too expensive. For example, material utilization is low in both vacuum evaporation and spin-coating deposition methods, and the former also

Table 1 The material costs in the polymer solar cells

	Spin casting ($/inch^2)	Slot/Blade coating ($/inch^2)	Slot/Blade coating (ITO-free) ($/inch^2)	Slot/Blade coating (ITO-free and evaporation-free) ($/inch^2)
ITO	0.20	0.20	–	–
Ink (PEDOT, Active, etc.)	0.060 + 1.200	0.003 + 0.060	0.003 + 0.060	0.003 + 0.060 + 0.002 (Ag ink)
Aluminum	0.104	0.104	0.104	–
Total cost (inch^2)	1.564	0.367	0.167	0.065

requires expensive vacuum facility. Thus, to meet the requirements of throughput and material utilization, various practical and efficient coating methods such as roll-to-roll, blade coating, spray coating, and slot-die coating are being developed and reported. Here, we give an estimate of the material cost for making OPVs, which was calculated per inch^2-area device. Because there is little waste of solution in the blade/slot coating process, the volume of the solution consumption is 20-fold less than that of spin coating. For instance, the blade coating having an ink supplying nozzle utilizes 30 μl solution for a 2″ × 3″ size substrate. On the other hand, spin coating requires more than 500 μl to cover the same area substrate, clearly not suitable for large-scale manufacturing process considering the high material cost of electronic materials. Another consideration is the ITO transparent conductor commonly used for organic electronic devices: even though it has good transparency and high conductivity, its cost has increased significantly due to the worldwide demand and production of LCD and OLED displays, and touch panels along with the fact that the indium is a relatively scarce element on the planet earth. In fact, ITO coated glass accounts for 12 % (spin coating) and 54 % (slot coating) of the whole device cost as shown in Table 1. Moreover, the flexible ITO-PET is more expensive than ITO-glass and occupies 35 % in an electronics device application [5]. To achieve 1$/W target in the polymer solar cells, the cost of transparent conductors and the active materials during the process should be reduced.

1.1 Various Printing/Coating Technologies for Polymer Electronics

Among conventional printing/coating technologies, the roll-to-roll printing, gravure, flexography, and offset printing offer great productivity compared with other manufacturing technologies (Table 2). However, whether these conventional printing processes are appropriate for manufacturing polymer electronics should be considered. For instance, screen printing is a simple printing process but it is

Table 2 The printing parameters and features in conventional printing technologies

	Inkjet	Screen	Gravure	Flexo.	Offset
Resolution (μm)	16–50	30	20–75	75	30–50
Thickness (nm)	<100	>1000	<50 nm	<50 nm	<1000
Viscosity (mPa s)	<20	500–50000	50–200	50–500	20–100 k
Coating speed (m²/s)	0.1	<10	60	10	20
Polymer ink	○	○	○	○	×

limited by the requirement of high ink viscosity. Inkjet printing is useful for fine patterning and thinner film using less viscous solution, but due to its serial process nature it is not suitable for large area film coating. In terms of large area coating, roll-to-roll coating has more flexibility to be adapted for the various coating area and to obtain varied film thickness.

1.2 General Coating Characteristics in Coating Methods: Thickness Control

This section introduces and compares general coating processes such as spin coating, knife coating, and slot-die coating. Since film thickness and uniformity are more important factors for electronics devices than traditional coating industries, we will examine some equations to get a clear picture of the key parameters affecting the film thickness. We aim at understanding the general coating characteristics for the practical coating process.

1.2.1 Spin Coating

Spin coating is one of the most popular coating methods as it is simple and easy to realize the intended film thickness. The solution dispensed on the substrate can be spread by a centrifugal force and the wet film is thinned down during the spin process. The film thickness depends on the viscosity and concentration of the solution. However, the final thickness of the film is mainly controlled by the spin speed, and thinner film can be achieved at higher spin speed.

In the following equations h_w is the wet film thickness, x: rate of the solids contacting on the substrate, ω: angular speed, ρ: solution concentration, C: constant for the coating gas in the coating chamber, μ: viscosity of the solution. The wet film thickness can be expressed as follows:

$$h_w = x \left(\frac{e}{2(1-x)K} \right)^{1/3} \tag{1}$$

where $e = C\sqrt{\omega}$, and $K = \frac{\rho\omega^2}{3\mu}$.

When we consider the evaporation of the solvent during the coating process, the final film thickness can be expressed as follows:

$$h_f = xh_w$$

and finally [6],

$$h_f \propto x \left(\frac{\mu}{\rho\omega}\right)^{1/2} \tag{2}$$

Therefore, the film thickness can be precisely controlled by the parameters in Eq. (2). However, very small amounts of the solution remain on the substrate to form the film during the spinning process. The rest of the solution is totally wasted. As a result, material utilization in the spin-coating process is commonly too low, sometimes less than 5 % of the solution volume. Therefore, spin coating is not considered as a practical manufacturing process.

1.2.2 Blade (Knife-Edge) Coating

The blade-coating method is commonly used in various coating industries and generally referred as knife-edge coating. The amount of solution (metered or not metered) is dispensed ahead of the blade, and the blade moves with a given speed as shown in Fig. 2. Contrary to spin coating where the film thickness is inversely proportion to the spin rate, the film thickness in the blade coating increases with the blade speed (V_{blade}). The film thickness in blade coating is also related to viscosity of the solution μ, surface tension of the solution, and curvature radius of the downstream meniscus R [7].

$$h = 1.34 \left(\frac{\mu V_{\text{blade}}}{\sigma}\right)^{2/3} R \tag{3}$$

The downstream meniscus can be expressed with pressure difference between P_1 and P_2.

$$h = 1.34 \left(\frac{\mu V_{\text{blade}}}{\sigma}\right)^{2/3} (P_2 - P_1) \tag{4}$$

Thus, the film thickness in the blade coating increases with blade speed, because as the blade moves faster, it has less chance to remove the solution on the substrate with the other parameters fixed. The volume of the moving bead will be smaller in the high-speed blade coating. Therefore, a large amount of solution will remain on the substrate after the blade and result in a thicker film. In the same

Fig. 2 The schematic diagram of the blade-coating process
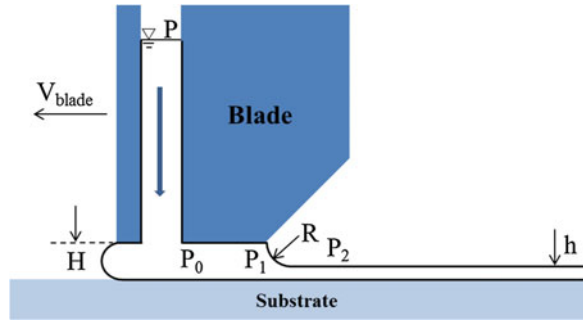
manner, if the surface tension is small, a large amount of volume will stay after the coating. This phenomenon is also known in the dip-coating process, where the typical film thickness equation is expressed as [8],

$$h = 0.946 \left(\frac{\mu V_{\text{blade}}}{\sigma} \right)^{1/6} \left(\frac{\mu V_{\text{blade}}}{\rho g} \right)^{1/2} \tag{5}$$

If the density of the solution ρ, viscosity μ, and surface tension σ are treated as constants, we can lump them together as a coating constant K. Similar treatment can be applied to blade coating. Therefore in both cases the film thickness versus blade speed can be expressed simply as

$$h \cong K(V_{\text{blade}})^{2/3} \tag{6}$$

In the actual blade-coating experiment, we found that the film thickness of P3HT:PC$_{61}$BM blend film used as the active layer (substrate size: $2'' \times 3''$) in the polymer solar cells is well matched with theoretical values as shown in Fig. 3. The solution consisted of 20 mg P3HT and 16 mg PC$_{61}$BM dissolved in 1.2 mg dichlorobenzene.

1.2.3 Slot (Die) Coating

If there is no pumping pressure to deliver the ink from the reservoir to slot nozzle, the thickness relation is the same as that of blade coating. However, conventional slot coating uses the static pump to extrude the solution. Therefore, the thickness depends on the volume-rate of the pumped solution. The thickness can be expressed as follows:

$$h_w \simeq \frac{\dot{V}}{W V_{\text{slot}}} \tag{7}$$

$\dot{V}$: volume flow rate of the pumping, W: coating width of the slot-die, V_{slot}: coating speed.

Fig. 3 The relationship between the various film thicknesses of the P3HT:PC$_{61}$BM layer and the blade speeds
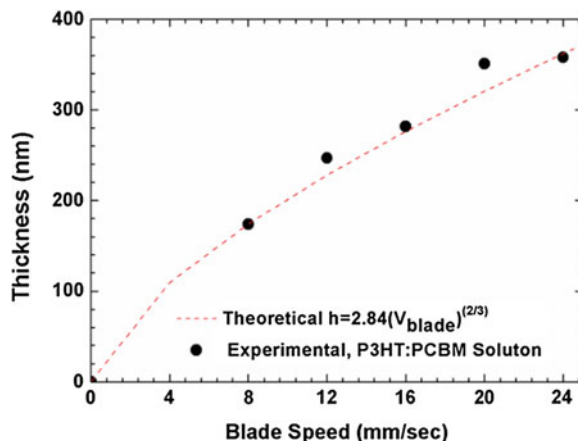

1.3 Coating Instabilities

In typical roll-to-roll coating process such as gravure coating, the surface of the printing rolls has many engraved cells. A picture of the gravure coating system is shown in Fig. 8. The ink in the engraved cell on the roll surface is transferred to substrate in the roll-to-roll coating, while there is direct contact between the gravure roll and the substrate (in comparison with blade or die coating where a fluid layer exists between the two rolls, and later will be referred as non-contact coating process). The direct contact mechanism of the ink transfer causes printing/coating instability, such as in the form of streak patterns in the film as shown in Fig. 6. The small amount of the ink in the gravure cell moves like an extensional viscous flow during the ink transfer. The extended viscous fluid causes irregular streak patterns. An example is shown in Fig. 4 for the emissive polymer solution/material. This coating instability can be explained by the capillary number, C_a. This dimensionless number is defined by the surface energy and viscosity of the solution.

$$C_a = \frac{\mu V}{\sigma} \qquad (8)$$

μ: the viscosity of fluid, V: the flow rate (roll speed), σ: the surface tension. Typically, larger C_a will cause coating instabilities, such as ribbing, cascading, and coating mist, due to the cavitation.

The viscosity of the solution increases for higher molecular weight material. For instance, the emissive polymer in the light-emitting diodes has relatively high molecular weight around 1,000,000. Therefore, the coating problem can be more severe. Generally, viscosity also increases with the solution concentration, which

Fig. 4 The image of the irregular coating streaks (*yellow patterns*) with the thermally deformed aluminum cathode (metallic *bubble-like patterns*) due to the leakage current. The aluminum cathode was peeled out from the polymer light emissive layer after the device test
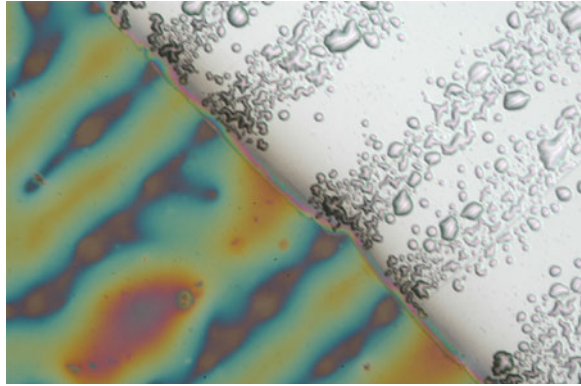
leads to higher capillary number and instability. Reducing the solution concentration, the film quality can be improved as shown in Fig. 5. To improve the film coating quality, the capillary number should be controlled by, e.g., reduction of coating speed or viscosity. However, the desired film thickness may not be achievable. Therefore, the contact coatings causing the extensional viscous flow of the polymer solution between the roll and substrate have more serious instability issues. The instability analysis can also apply to the coating processes such as blade coating where the blade does not have direct physical contact with the substrate (and hence will be referred to as non-contact coating). Because the blade or the slot-die coatings do not cause extensional viscose flow, they are frequently more suitable choices.

In the case of low-band gap polymer semiconductor (iI-T3) [9] dissolved into dichlorobenzene, because the solution has very low surface tension, the capillary number depends highly on the coating speed. Coating meniscus can be broken due to low cohesive energy of the solution under fast coating condition, showing as irregular patterns due to instability. On the other hand, the coating quality of the low-band gap polymer will be improved by reducing the coating speed as shown in Fig. 6.

There is another important parameter to determine the coating instability. It is the leveling time for the solvent in the wet film to be evaporated after the coating process. If the solvent evaporates relatively slowly, the film can be self-leveled under the surface tension, and the irregular coating pattern resulted from the instability will disappear by the flow itself.

The wet film thickness containing the instability can be considered as a simple wave with amplitude δ and characteristics wavelength $(2\pi/q)$ as follow (Fig. 7):

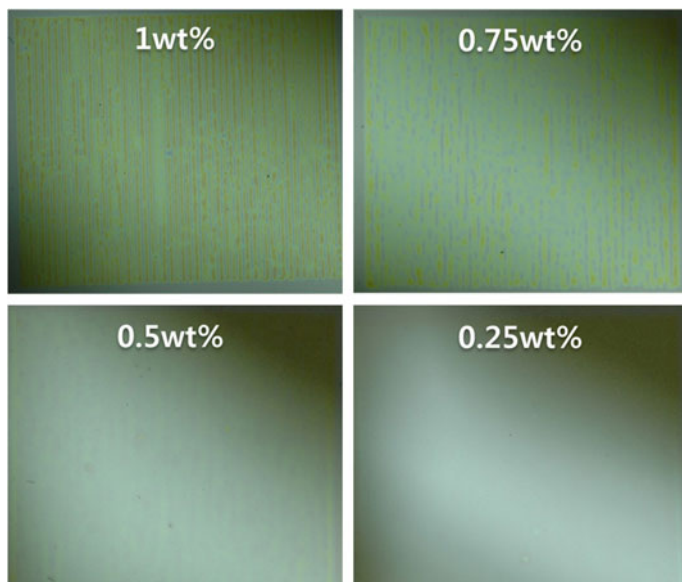$$e = e_0 + \delta e \cos(qx) \tag{9}$$

Fig. 5 The irregular coating patterns in the emissive material due to instability with respect to the solution concentration, 1, 0.75, 0.5 and 0.25 wt%. The lower concentration improves the film quality, the irregular pattern disappear in the case of 0.25 w%. The other coating condition are 80 m/min, 200 LPI (line per inch), 22 μm of the gravure cell depth
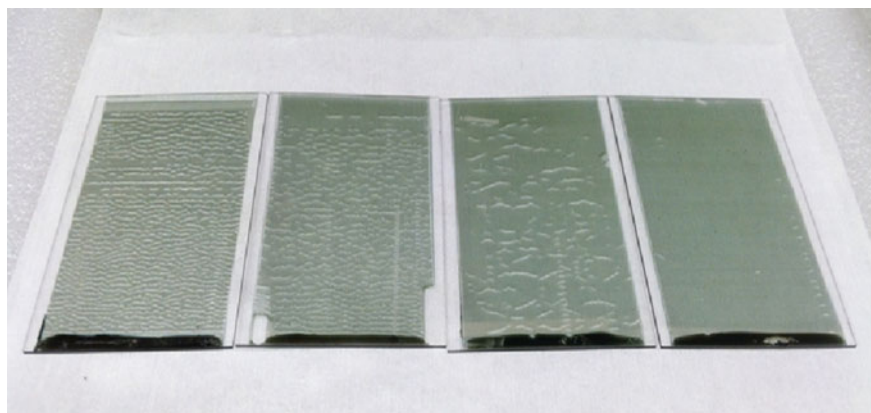

Fig. 6 The irregular coating patterns in iI-T3:PC$_{71}$BM blend PV material due to instability with respect to the blade-coating speed, 20, 16, 12 and 8 mm/s. Clearly lower speed removes instability and leads to uniform film
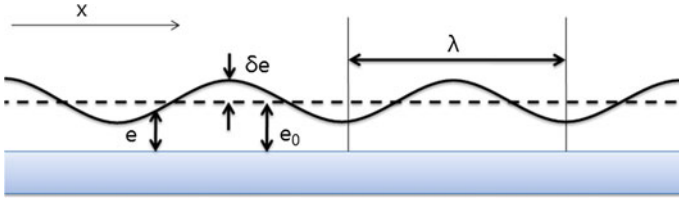
Fig. 7 The ideal modeling of the coating ripples of the wet film solution

The film thickness variation, expressed as δ, will be reduced by the self-leveling flow. We estimate the leveling time τ. First the fluid speed (v) can be deduced from the 1-dimensional Navier–Stokes equation. Then the flow rate Q can be deduced from Young–Laplace equation:

$$-\frac{\partial p}{\partial x} + \mu \frac{\partial^2 v}{\partial z^2} = 0 \tag{10}$$

$$Q \approx \frac{e_0}{\mu} \sigma q^3 \delta e \sin(qx) \tag{11}$$

Considering the volume conservation,

$$\frac{\partial Q}{\partial x} = -\mu \frac{\partial e}{\partial t} \tag{12}$$

$$\frac{\mathrm{d}\delta e}{\mathrm{d}t} = -\frac{\delta e}{\tau} \tag{13}$$

Solving the differential equation yields the leveling time as follows:

$$\tau = \frac{\mu \lambda^4}{\sigma e_0^3} \tag{14}$$

If leveling time is smaller than evaporation time, the pattern will disappear due to the leveling flow. However, if the leveling time is too long or evaporation time too fast, the irregular pattern will remain. The leveling time depends on the viscosity and surface tension of the solution. For instance, when the viscosity of the given polymer solution is 100 mPa s, the surface tension is 25 m N/m, the characteristic pitch of the stripes is 500 μm, the wet film thickness is 10 μm, and the leveling time will be 250 s. To remove the irregular patterns, the solvent having higher boiling temperature should be considered. By choosing a solvent that can evaporate slowly beyond the leveling time, flat and uniform films can be produced (Fig. 8).
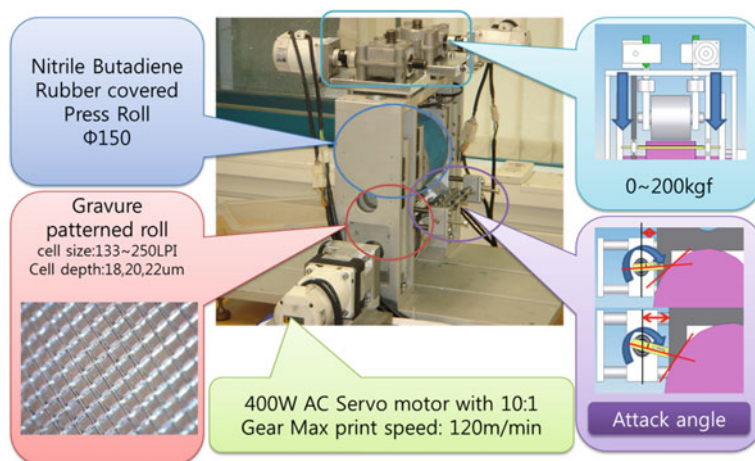
Fig. 8 The gravure coating system and its coating parts

Uniform film is important to ensure proper device function. Example, the streak patterns of the emissive material shown in Fig. 9 can cause electrical shorting problems under the bias voltage. This unwanted streak pattern can be controlled by adjusting the printing speed and ink viscosity. The viscosity of the solution can be reduced by diluting the solution as discussed earlier for the emissive polymer. For another example, the commonly used conductive polymer PEDOT:PSS solution is also difficult to form a uniform film on the polymer substrate as shown in Fig. 10. In this case, since the solution is water-born and hydrophilic solution, it is difficult to coat uniformly. The irregular pattern of the PEDOT:PSS layer can be controlled by adding isopropyl alcohol (IPA) solution to reduce viscosity. Dilution with IPA has better effect than that of adding a surfactant. However, it is hard to obtain an appropriate film thickness by one time coating using a lower concentration solution. Therefore, in the case of using the viscous solution, the film quality is sensitive to the coating instability caused by ink transfer in the contact coating method. Due to the basic problems of the contact coating process, non-contact coating methods will be introduced. Slot-die coating as a typical non-contact coating is a good manufacturing tool for the large scale solar cells.

2 Characteristics of Roll-to-Roll Coated Functional Layers Toward the Large Scale Devices

This section describes the roll-to-roll/blade-coating process with applications in large area OPV and OLED devices. We discuss the requirements of the functional layers (e.g., transparent electrode, hole extraction layer, charge separation layer,
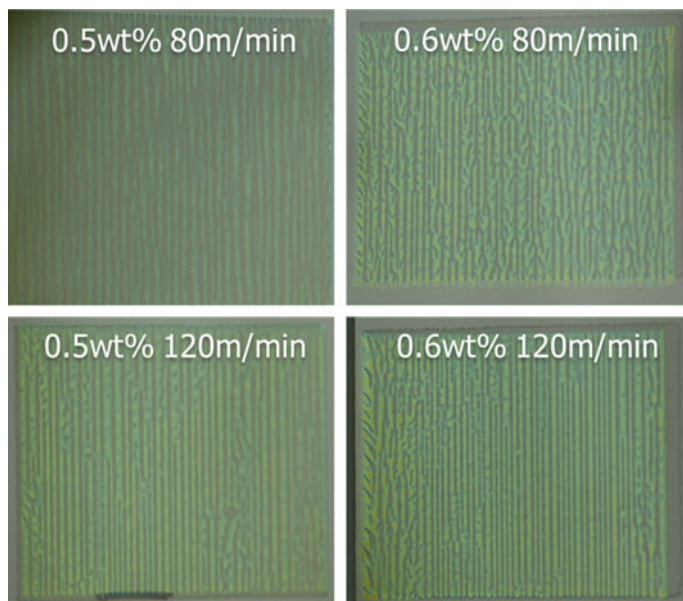
Fig. 9 The irregular streak patterns of the emissive layer in PLEDs with respect to the different concentrations and coating speeds

electron transport layer, and electron extraction layer) in terms of the coating performances such as coating thickness, uniformity, and electrical properties.

2.1 Roll-to-Roll and Blade-Coating System as the Noncontact-Coating Methods

Among the various printing processes to make large area polymer PVs and PLEDs, the roll-to-roll coating system is one of the most favorable candidates. By adding a facile doctor blade to the roll-to-roll system, a simple, noncontact coating platform can be constructed, where the blade does not contact the substrate directly but via a liquid layer. As compared with the slot-die system, it is a valuable tool for fabrication of large-sized thin films.

Since the conventional blade-coating system has advantages such as easy operation, simple structure, and low cost, it has been widely used in not only laboratory but also industrial scale. Previously, there have been efforts to make organic electronics using simple blade coating due to these advantages. However, there is a serious problem in the conventional blade-coating process: because the ink supplying is not homogeneous, the layer thickness varies: the initial layer thickness was frequently thicker than the final layer thickness. In addition, the ink supply in the slot-die coater relies on the use of external pumping, which cannot be
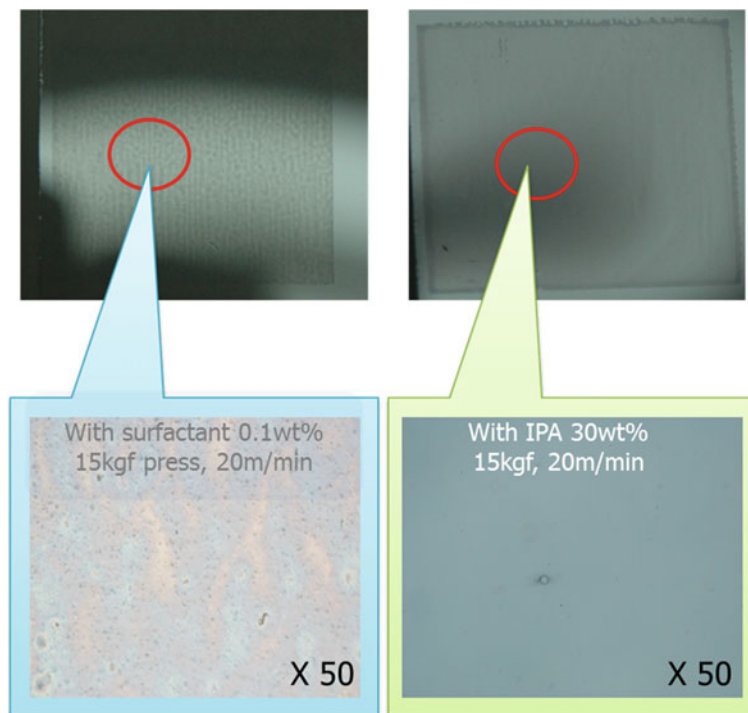
Fig. 10 The control of the irregular streak patterns by adding surfactant (Dynol 604, Air product inc.) and isopropyl alcohol (IPA)

thin enough, e.g., for the electron injection layer using the low-viscous solutions. To address the nonuniform film thickness problem, a pre-metering mechanism, or nozzle system should be added like that used in a slot coating. In order to achieve better film uniformity for much thinner organic layers such as the electron injection layer in PLED and to solve the fundamental ink supplying problem, we attach a simple slide glass to the blade surface to meter the solution. The whole system was developed with 8″-based rollers and it is driven by an AC servo-motor. As shown in Fig. 11 the solution contained in the slit between the glass plate and the blade flows and created a meniscus in front of the glass, followed by a homogeneous laminar flow at the back of the blade. This fine laminar flow is the key to uniformity and better film quality. The control variables of the film thickness are the blade gap, the slit gap, the blade speed, the ink concentration, and the surface energy of the substrate, and the slit.

The blade-slit coating method utilizes only the gravity of the solution for the ink supply, the flow rate can be minimized effectively. The estimated minimal thickness of the blade-slit coating is around a few nanometers. The minimal wet film thickness in the slot-die system is around 1 μm, and the estimated dry film thicknesses are few tens of nanometers. Because the device performance sensitively depends on the film thickness in the organic electronics, the thickness of each layer should be controlled
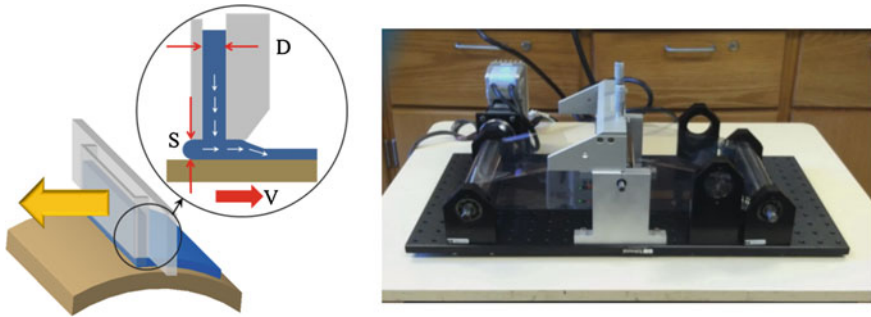
Fig. 11 The schematic diagram of blade-slot coating showing the ink supply and coating flows; and a 8″ based roll-to-roll coating system

fairly accurately to optimize the device performance. When designing the various device structures by the solution coating processes, special consideration should be given to whether each layer thickness can be realized by the practical coating method such as the blade/roll-to-roll coating equipment.

2.2 Conventional Device Structure in the PLEDs

We now discuss the roll-to-roll fabrication of PLEDs. A typical PLEDs is indium tin oxide (ITO)/Hole transporting layer/Emissive layer/electron transporting layer/ metal cathode, poly(3,4-ethylenedioxythiophene)poly-(styrenesulfonate) (PEDOT: PSS) conductive polymer is a commonly used hole transporting layer. Phenyl substituted poly(para-phenylene vinylene)—known as "Super Yellow," (will simply be referred as S-Y, Merck, PDY-132) will be used as yellow light-emitting layer. Zinc oxide (ZnO) nanoparticle (NP) is used as electron transporting layer, and Al as cathode, poly(ethylene oxide) (PEO), and tetra-n-butylammonium tet-rafluoborate (TBABF$_4$) in acetonitrile (ionic solution) is used to induce a dipole layer to adjust the work function of the cathode, as shown in Fig. 12 [10].

2.3 Flexible and Transparent Electrode for Large-Scale PLEDs

2.3.1 Optical and Electrical Property of the Roll-to-Roll Coated Polymer Electrode

Since indium tin oxide (ITO) has good optical and electrical properties, it has been commonly used as a transparent electrode in displays and solar cells. However, the cost of the ITO is expensive and mechanical bending strength is poor due to its
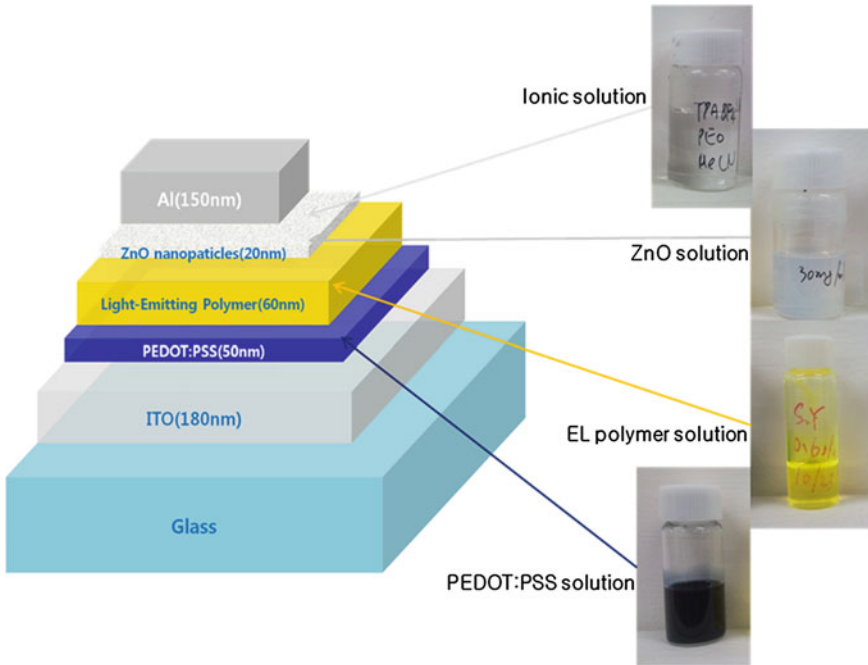
Fig. 12 Illustration of the multilayer structure and the solutions of the functional layers

brittleness. Moreover, the flexible ITO sputtered on PET substrate has less transmittance and conductivity than that of the ITO-glass. There are many candidates for the alternative transparent electrodes such as metal mesh, silver nanowire [11], graphene [12], carbon nanotubes [13], and conducting polymer [14]. The conducting polymer of PEDOT:PSS fabricated by roll-to-roll coating offers satisfactory optical transparency and electrical conductivity (Fig. 13) as polymer anode. For example, a 200 nm thick polymer anode (PEDOT:PSS, H.C. Stock PH1000) can be coated by roll-to-roll blade-slit coating method over large substrate at one time without wasting of the solution as shown in Fig. 14. In comparison, spin coating method requires three time coatings and wasting lots of solutions to cast the same 200 nm thick polymer anode. The sheet resistance of the polymer anode made by roll-to-roll coating is around 40 Ω/sq, when the thickness is 250 nm. The transmittance including PET substrate of the polymer anode is 74 % at 550 nm wavelength. For a thinner, 120 nm thick polymer anode, the sheet resistance is 110 Ω/sq and the transmittance is around 85 %.

Fig. 13 Comparison of transmittance between ITO-PET and R2R coated PH1000 (42 and 112 Ω/sq) in the visible wavelength range. Reproduced from [15] with permission of Wiley-VCH Verlag GmbH & Co. KGaA © 2013
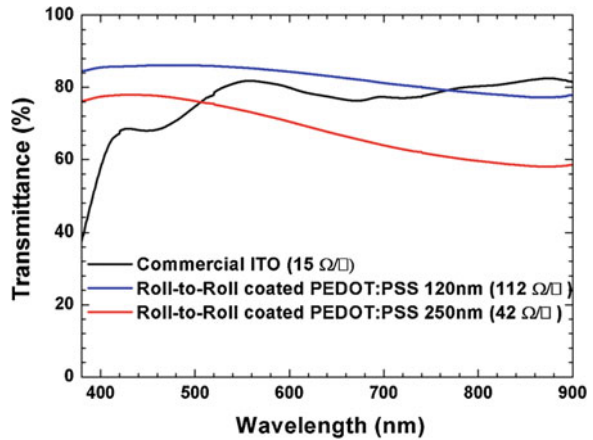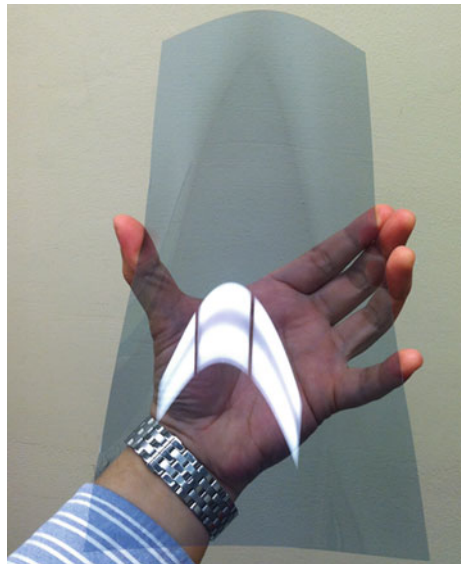

Fig. 14 The roll-to-roll coated polymer anode (PH1000) on the 8″ flexible PET substrate

2.3.2 The Mechanical and Stability of the Transparent Polymer Electrode

The polymer electrode has better bending strength than ITO-PET as shown in Table 3. The variation of the sheet resistance of the film is less than ITO-PET. The ITO-PET is vulnerable to the bending stress: extensive cracks are developed if the ITO surface is subject to just one time excessive bending stress. Thus in the case of PLED, we could not observe the light emission from the device after the several bending cycles.

Table 3 The sheet resistance change of conducting polymer anode and ITO-PET following the change in bending angle

	0°	30°	60°	90°	120°	150°	180°
ITO PET (Ω/sq)	13.9	17.6	26.1	40.3	52.6	68.2	309.3
Polymer anode (Ω/sq)	68.8	69.0	69.0	69.1	69.2	69.5	69.7

The sheet resistance of ITO is significantly increased when the bending angle is increased. In contrast, the conducting polymer shows almost the same sheet resistance. Reproduced from [15] with permission of Wiley-VCH Verlag GmbH & Co. KGaA © 2013

2.3.3 Coating Evaluations of Functional Layers in the PLEDs

For large-scale devices, the thickness of the blade-only coating is nonuniform in the coating direction. Accordingly, the layer thickness in the initial state is usually greater than that in the final state for a large-scale device. Thickness variation is a serious problem associated with PLEDs, because difference in the functional layer thickness, in particular the very thin electron injection layer causes variation in the luminance in different areas. The final thinner area will be brighter than that of initial thicker area as shown in Fig. 15. Furthermore, an excessively thin area can even cause electrical shorts in the PLED layers.

Coating of the active layers in PLEDs using the blade-slit coating system can effectively address the above issues. The coating mechanism is similar to the slot-die coating. The main difference between the two is the ink supply. Organic electronic devices such as OPVs, OTFTs, and OLEDs have thin layers (from a few nanometers to a few hundreds of nanometers). Thus, it requires smaller feeding capacity of the solution than what typical slot-die coater delivers. Especially in the PLEDs illustrated above, the ZnO NP layer/Ionic complex layer as the electron transport/electron injection layer is even thinner: the total thickness of the two layers is only from 15 to 30 nm. Therefore, it requires less and homogeneous amount of ink supply. In this effort, we aimed at fabricating not only the hole injection layer, emissive layer, and electron transport layer but also the much thinner electron injection layer using the new blade-slit coating method. The blade-slit coating system we developed does not employ external pumping system, but utilizes only natural gravity and surface tension of the solution to flow out from the capillary to the surface of the substrate, which can effectively reduce the flow rate and the wet film thickness.

The following is a summary of the fabrication process. Each layer was fabricated at a temperature of 45 °C on the hot plate under ambient air conditions. The blade-slit speed was 15 mm/s. Sputtered ITO glass (15 Ω/sq) was cleaned beforehand by ultrasonic treatment in pure water, acetone, and IPA. It was then subjected to a UV-ozone treatment for approximately 1 h. A PEDOT:PSS layer (40 nm) was blade-slit coated onto the ITO glass, where the slit gap between the blade and the slide glass was 70 μm. The yellow light-emitting polymer (S-Y) dissolved in toluene at 0.6 wt% was then blade-slit coated (approximately 75 nm), with the slit gap of 210 μm. The ZnO NP layer (approximately 30 nm) was
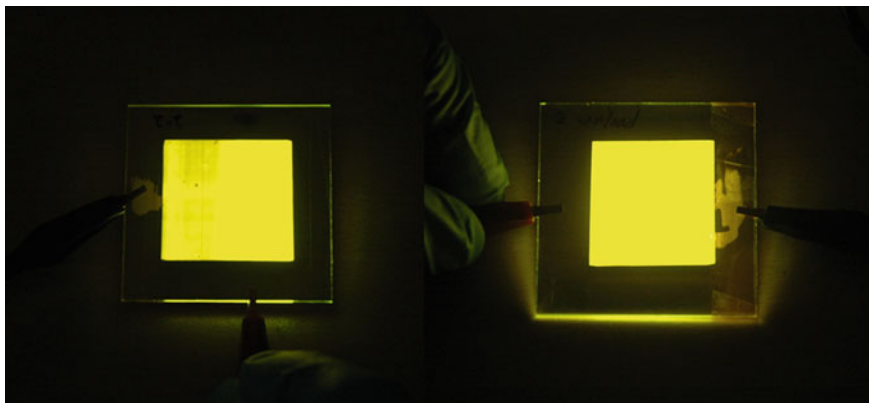
Fig. 15 The light-emitting images of the blade-coated devices, non-uniformly coated by the only blade coating (*left*) and uniformly coated layer utilizing the slit nozzle

blade-slit coated onto the emissive layer, with a slit gap of 210 μm. Finally, the ionic solution was blade-slit coated onto the ZnO NP layer, with the slit gap of 350 μm. The ZnO NPs dispersed solution, dissolved in 1-butanol at a concentration of 30 mg/mL, was synthesized according to the method described by Beek et al. [24] The ZnO NPs appeared rather monodispersed with an average size of approximately 5 nm. The ZnO NPs layer was thin and porous, which allows the ionic solution containing TBABF$_4$ and PEO to permeate into the porous ZnO NP layer. The aluminium cathode (100 nm) was thermally evaporated under 2×10^{-6} torr in this demonstration, but could be replaced by the blade-coated Ag paste. The film uniformity of the emissive layer is easily verified by UV-light exposure as shown in Fig. 16. However, the other layer should be measured by surface profiler or SEM image. The amount of the solution for each layer to be coated is only 25 μL in area of 50 mm × 50 mm. The whole volume of the slit space is 550 μL. In addition, it is inexpensive and easy to change and clean the nozzle for the different solutions. The blade-slit coating employs transparent slide glass for the slit capillary, which is quite useful to observe the fluids flow in the slit nozzle.

2.3.4 Uniformity of the Functional Layers in PLEDs Coated by Blade-Slit Coating

As stated, the blade-slit coating improved the coating uniformity in the moving direction. The measured standard deviations of the blade-only coated PEDOT:PSS (hole injection layer) and Super Yellow (yellow light-emitting polymer, structure shown in Fig. 17) layers were about 5.7 and 5.7 nm, respectively, representing a nonuniformity of 7.9 and 9.1 %, respectively, of film thickness. These were calculated from thickness data measured at ten given positions (2 columns and 5 rows, each spaced 25 and 12 mm, respectively) in the area of the coated layer
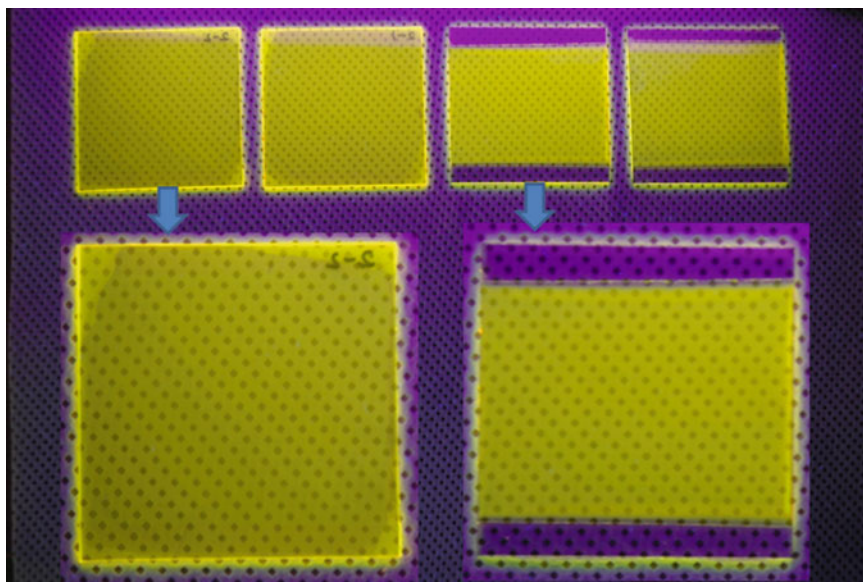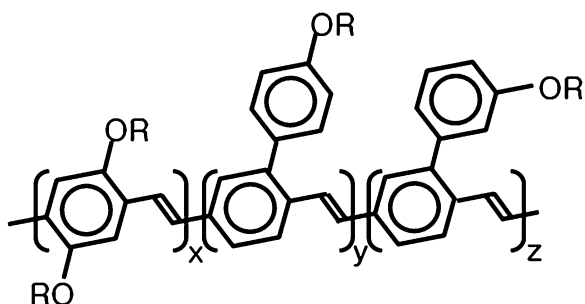
Fig. 16 The UV-light irradiation for evaluation of the coating quality in the emissive layer, *left* films are spin-coated and *right* films are blade-coated films

Fig. 17 Molecular structure of the *yellow* light-emitting phenyl substituted poly(phenylene) vinylene

(substrate area: 70 mm × 80 mm). The lack of the uniformity of the blade-only coated layers created serious nonuniform luminance when the device was driven electrically. In comparison, in the blade-slit coated layer the standard deviation was only 0.68 and 2.3 nm for the PEDOT:PSS and emissive layer S-Y. So non-uniformity is only 2.1 and 2.2 % of their respective layer thicknesses (Table 4). It exhibited dramatic improvement in film uniformity compared to the blade-only coating. The electrical performances of PLED devices made of polymer anode are discussed in Sect. 3.

Table 4 Film uniformity of PEDOT:PSS and super yellow layers for blade-only coating versus blade-slit coating

		1	2	3	4	5	6	7	8	9	10	Avg[a] (nm)	SD[b] (nm)	U[c] (%)
Blade-only	Hole injection layer, PEDOT:PSS (nm)													
	Pos[d]	1	2	3	4	5	6	7	8	9	10			
	Thk[e]	73.1	79.3	71.6	76.7	75.0	78.0	73.3	61.1	63.2	73.1	72.4	5.7	7.9
	Light-emitting layer, super yellow (nm)													
	Pos[d]	1	2	3	4	5	6	7	8	9	10			
	Thk[e]	71.3	55.8	58.1	55.9	60.2	71.4	60.9	64.7	68.9	60.2	62.7	5.7	9.1
Blade slit	Hole injection layer, PEDOT:PSS (nm)													
	Pos[d]	1	2	3	4	5	6	7	8	9	10			
	Thk[e]	32.9	32.4	32.2	33.3	31.3	33.7	32.6	32.0	31.9	32.0	32.4	0.68	2.1
	Light-emitting layer, super yellow (nm)													
	Pos[d]	1	2	3	4	5	6	7	8	9	10			
	Thk[e]	102.2	100.0	102.9	105.4	104.3	102.2	100.2	100.1	106.1	105.7	102.9	2.3	2.2

Reproduced from [16] with permission from Elsevier © 2012

[a] *Avg*: average thickness of ten points (nm)
[b] *SD*: standard deviation (nm)
[c] *U*: non-uniformity (%): (SD/Avg)
[d] *Pos*: measured position
[e] *Thk*: thickness

Table 5 Thickness variations of layers for blade-slit coating method with respect to gap distance between the blade and substrate

Super yellow		ZnO nanoparticle	
Blade gap (μm)	Film thickness (nm)	Blade gap (μm)	Film thickness (nm)
30	60.0	45	15.3
35	75.0	55	20.4
40	91.0	65	30.0

Reproduced from [16] with permission from Elsevier © 2012

### 2.3.5 Solution Processable Electron Transport/Injection Layer

Low-work-function metals or compounds such as LiF, CsF, NaF, Cs_2CO_3, Ca, Ba, and Mg have often been used as electron injection/extraction layer [17–23]. In spite of the use of lithium fluoride and aluminium bi-layer cathodes, these alkali or alkaline-earth metal-halides as electron injection materials are still sensitive to oxygen and moisture, resulting in degradation of the OLEDs and consequently shorting their lifetimes. The ZnO NP layer used here is not only a stable electron injection layer but can also be fabricated by the solution coating process. In particular, the interface dipole formed by the $TBABF_4$ and PEO ionic liquid significantly lowers the electron injection barrier. Therefore, the ZnO NP and the ionic interlayer are appropriate for the solution process [10]. Because the ZnO NP layers were too thin to evaluate by the surface profiler, the coating thickness, and uniformity of the film were investigated with scanning electron microscopy (SEM). The film thickness of the ZnO NP layer was again controlled by the blade gap distance. The thickness of the ZnO NP layer, using a 30 mg/mL ZnO solution, was increased from 15.3 to 30.0 nm when the blade gap was increased from 45 to 65 μm. See Table 5. Surprisingly, the very thin ZnO NP layers can also be controllably coated using our blade-slit coating system.

2.4 Experimental Characterization of Polymer Light-Emitting Diodes

The device structures of the PLEDs are shown in Fig. 12. The device performance characteristics of the J (current density), V (voltage), L (luminance) curves were obtained from a Minolta CS-100 luminance meter and a Keithley 2400 source meter. The measurement process was conducted in ambient air conditions without encapsulation.

The control PLED devices were also fabricated by the spin coating process because it is easier to do on a small scale and also offers high efficiency. For a more accurate and fair comparison of blade-slit coating and spin coating, the layer thicknesses of the two devices were kept similar. As a result, the turn-on-voltages
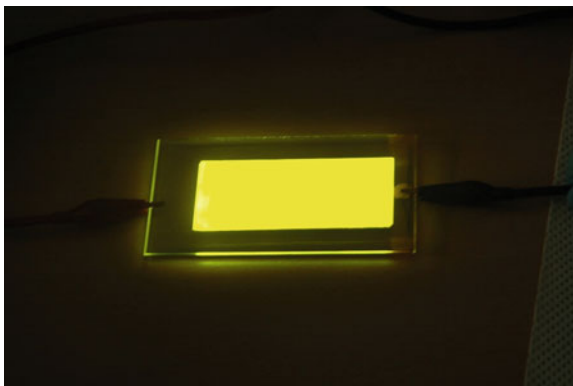
and the maximum luminance voltage of the two devices were almost the same, as
shown in Fig. 19a, indicating the blade-slit coating method can realize the same
coating quality as that of spin coating but easily covers larger areas. In addition,
Fig. 19b compares the performance (in terms of luminescence intensity) between
the spin-coated devices and blade-slit coated devices. Though the blade-slit coated
device was made in the air environment, the luminous efficiency of the blade-slit
coated PLED reached 5.26 cd/A. The luminous efficiency of the spin-coated
device fabricated in the Nitrogen-filled glove-box was 6.30 cd/A. These compa-
rable results support the advantage of the blade-slit coating method, which is easier
and less wasteful for materials for large-sized devices (100 mm × 50 mm) as
shown in Fig. 18. Furthermore, the luminous efficiency of the PLEDs using the
ZnO and ionic surfactant (6.30 cd/A) are over two-fold higher than that using Ca
transporting layer (3.01 cd/A) as shown in Fig. 19b. The turn-on voltages of the
two devices are almost the same as 2.2 V as shown in Fig. 19a. Since the peak
emission wavelength of the S-Y is 560 nm as shown in the EL-spectra in Fig. 19c,
the optical band gap of the S-Y is calculated at 2.2 eV, the same as turn-on
voltage. This means that the devices have good electrical contact with Al cathode.
In addition, it reveals that the ammonium ions can be effectively incorporated into
the electron injection layer which lowers the electron injection barrier.

2.4.1 Roll-to-Roll Processed PLEDs

In this section, we show that the polymer anode (see Sect. 2.3) is superior to the
ITO-PET in making flexible PLEDs and resulting in higher PLEDs performance.
To evaluate the performance between the two devices, the two type devices were
fabricated using the same process, and with similar film thicknesses. As a result,
the turn-on-voltages and voltages at the maximum luminance of the two types of
devices were very similar (Fig. 20a). It implies that the thickness of each layer in
the two devices is about the same. The maximum luminance of ITO anode PLEDs
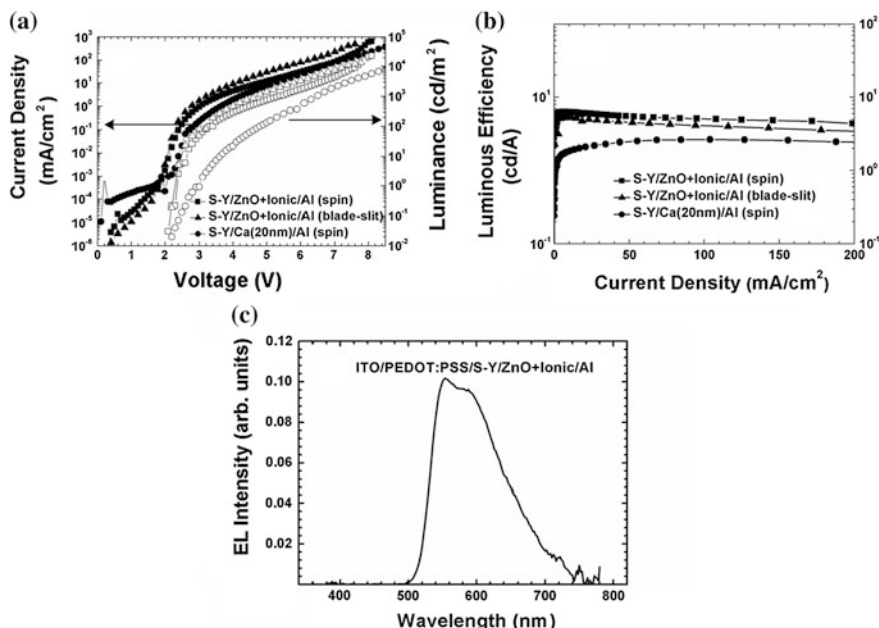was greater than that of polymer anode PLEDs. However, the maximum

Fig. 19 **a** Current density, voltage, and luminance (J-V-L) characteristics with the spin-coated, the blade-slit coated, and the spin-coated Ca (20 nm)/Al devices. **b** Luminous efficiency of the spin-coated, the blade-slit coated, and the spin-coated Ca (20 nm)/Al devices. **c** The electroluminescence spectra at a voltage of 5 V [16]
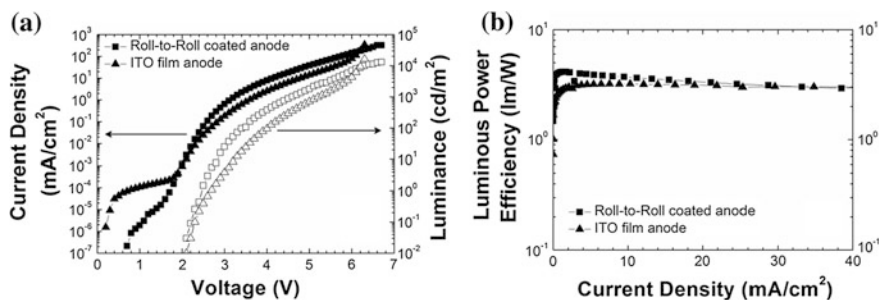

Fig. 20 The performance comparison of the ITO anode PLED and polymer anode PLED. **a** Current density, voltage, and luminance (J-V-L) characteristics with the ITO anode PLED and polymer anode PLED. **b** Luminous power efficiency of the ITO anode PLED and polymer anode PLED. Reproduced from [15] with permission of Wiley-VCH Verlag GmbH & Co. KGaA © 2013

luminance is only of secondary importance because commercialized devices are not driven at the extreme condition such as the maximum luminance. In this case, the PLED with polymer anode shows high performance in the range of commercial
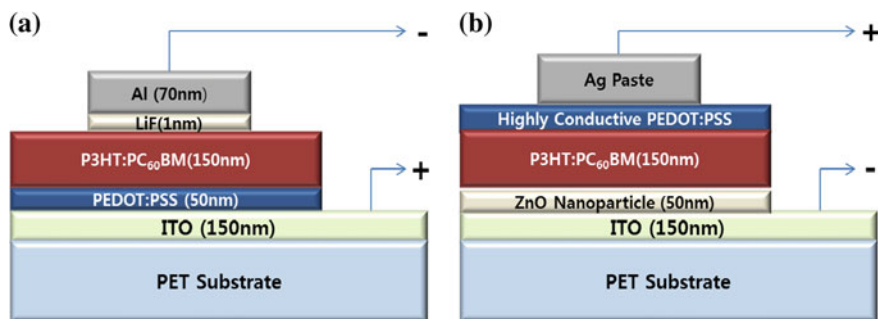
Fig. 21 The schematic diagrams of the two device structures, **a** bottom illuminated conventional structure and **b** bottom illuminated inverted structure

operation, about 2–6 V. In addition, the leakage current of the polymer anode PLEDs was lower than that of ITO anode PLEDs. That is because the polymer anode of PLEDs had improved surface roughness. The luminous power efficiency was 4.13 lm/W for PLED with polymer anode and 3.21 lm/W for that on ITO as shown in Fig. 20b. Consequently, the PLED made with polymer anode marked 28 % enhanced performance. This is because the polymer anode represents a higher transparency than the ITO around the wavelength of 560 nm, which is the emission peak in the EL-spectra of the SY. Furthermore, greatly suppressed roughness was important to enhance the device efficiency because it reduces leakage current between the anode and cathode.

2.5 Large-Scale Polymer Solar Cells

Two typical device structures of the polymer solar cells are shown in Fig. 21. The left one shows bottom illumination through transparent anode and is referred as normal type device. Such a device structure is not suitable for roll-to-roll processing as both LiF and Al layer will need vacuum deposition due to their high sensitivity to air and moisture, and LiF layer is extremely thin, of order 1 nm. The right one is refereed as inverted structure, and is suitable for low-cost fabrication. The whole functional layers can be fabricated by printing technologies such as roll-to-roll coating and screen printing.

2.5.1 Uniformity of the Functional Layers in OPVs by Blade Coating

The coating of PEDOT:PSS and ZnO NP layers as a hole extraction layer and electron transport layer in OPVs is the same as the PLEDs described in the previous section. The film uniformity by the blade-slit coating show better quality for the commonly used P3HT:PC$_{61}$BM (20 mg P3HT and 16 mg PC$_{61}$BM in 1.2 g

Table 6 Film uniformity of P3HT:PC$_{61}$BM blend film and iI-T3and PC$_{71}$BMblend film layers by spin-coating versus blade-slit coating

| Spin	P3HT:PC$_{61}$BM									Avg[a]	SD[b]	U[c]
Pos[d]	1	2	3	4	5	6	7	8	9	(nm)	(nm)	(%)
Thk[e]	350.2	278.8	327.3	337.7	265.7	318.4	328.3	277.8	317.1	311.3	28.1	9.0
Blade	P3HT:PC$_{61}$BM											
Pos[d]	1	2	3	4	5	6	7	8	9			
Thk[e]	247.1	249.2	252.5	266.1	212.6	236.1	264.7	253.1	287.9	252.1	19.7	7.8
Il-T3(Low-band gap polymer):PC$_{71}$BM												
Pos[d]	1	2	3	4	5	6	7	8	9			
Thk[e]	114.2	105.6	125.1	99.2	102.2	118.2	95.3	103.2	110.2	108.1	9.1	8.4

[a] *Avg*: average thickness of nine points (nm)
[b] *SD*: standard deviation (nm)
[c] *U*: nonuniformity (%): (SD/Avg)
[d] *Pos*: measured position
[e] *Thk*: thickness
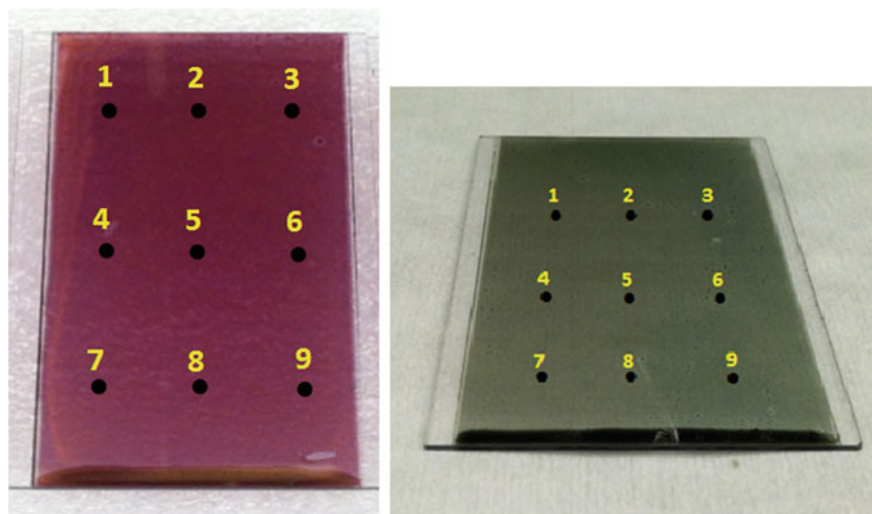
Fig. 22 P3HT:PC$_{60}$BM and low band gap Il-T3:PC$_{71}$BM blend films by blade-slit coating method and measuring points by surface profiler

dichlorobenzens) as described in Table 6. As another example, uniform film of a low band gap polymer iL-T3 (10 mg iI-T3 [9] and 15 mg PC$_{71}$BM in 1.0 g dichlorobenzens) coated by the blade-slit coating is also shown in Table 6 and Fig. 22. The thickness data were measured at nine given positions shown in Fig. 22 over the coated area of 50 mm $\times$ 75 mm. Furthermore, the film quality by the blade-slit coating is better than that by spin-coating as shown in Fig. 23. Since the surface quality of the film can affect the device performance such as shunt
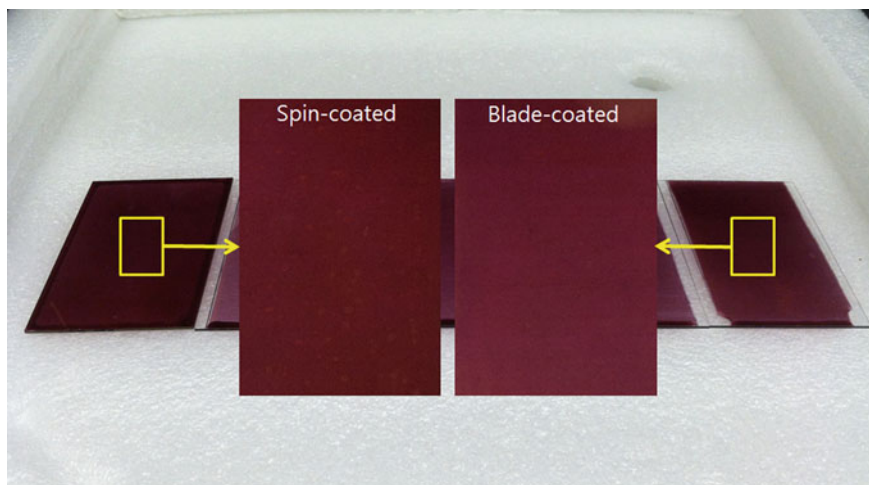
Fig. 23 The coating quality images of the blade-coated layers versus spin-coated layer. Defects can be seen in the latter

Table 7 The relationship between the blade speed and thickness of the P3HT:PCBM solution

Blade speed (mm/s)	8	12	16	20	24
Thickness (nm)	174.0	247.1	281.8	351.0	368.9

resistance and the fill factor, the overall power conversion efficiency will depend on the surface morphology. The film thickness can be controlled by modifying the coating speed. As discussed in the previous section, the film thickness is well matched by the theoretical relationship between the blade-coating speed and the film thickness as shown in Table 7. Higher speed leads to thicker film as shown in Fig. 24.

2.5.2 Device Performance in the Roll-to-Roll Processed Conventional Structure in Solar Cells

Conventional OPVs with the structure of ITO-glass/PEDOT:PSS/P3HT:PC$_{61}$BM/LiF/Al was fabricated as a control device. Among the functional layers, inorganic layers such as ITO, LiF, and Al cannot be coated by roll-to-roll process. However, the ITO can be replaced by polymer anode on PET substrate. The polymer anode was coated by roll-to-roll coating method. Low conductive PEDOT:PSS (AI4083) as a hole extraction layer and P3HT:PC$_{61}$BM donor-acceptor blend as polymer active layer were then roll-to-roll coated at air atmosphere. The layer thicknesses were 50 and 200 nm respectively. The LiF (1 nm) and Al (80 nm) were thermally evaporated in the vacuum chamber at a base pressure of 10^{-6} mbar.
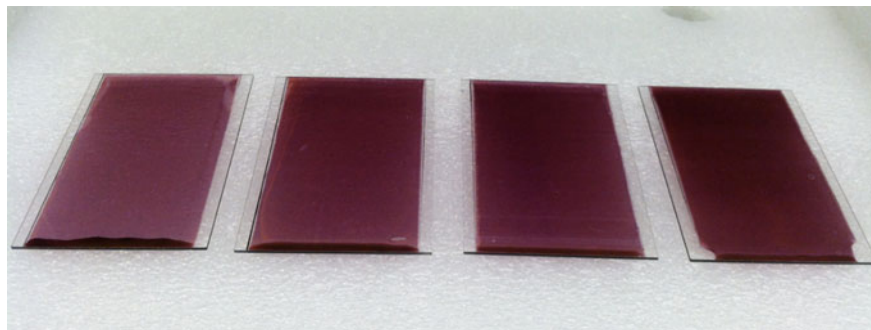
Fig. 24 The images of the blade-coated layers on the glass substrate (50 mm × 75 mm) with respect to the different coating speeds

Table 8 The performance of OPVs fabricated by the roll-to-roll coating

	Jsc (mA/cm^2)	Voc (V)	FF (%)	PCE (%)	Rs (Ω cm^2)	Rp (Ω cm^2)
50 Ω/sq	−13.63	0.59	36.71	2.26	30.00	174.06
150 Ω/sq	−10.59	0.59	42.66	3.43	20.07	196.25

Polymer anodes with two different thicknesses were used to make the OPVs. The device utilizing thinner polymer anode has 50 % higher series resistance than the thicker anode (200 nm) as shown in Table 8. The power conversion efficiency of OPVs using thicker anode was 3.43 %, while that using thinner anode (100 nm) showed less performance due to the series resistance even though it has similar shunt resistance (Fig. 25). The impact on the device efficiency for large-scale devices are discussed in detail in Sect. 2.5.6.

2.5.3 Device Performance of the Inverted OPV Structure

The typical inverted OPV structure is ITO-glass/interfacial layer/P3HT:PCBM/MoO3/Ag. We will examine the electrical performance for the different size devices. To fabricate the inverted OPVs, first ITO-glass was pre-cleaned by washing with DI water, acetone, and IPA, followed by O_2 plasma treated with 100 W for 1 min. The PEIE as the interfacial layer [27] and P3HT:PCBM layer was blade-slit coated except for the small area (1 mm diameter) control device which was spin-coated in the air atmosphere. The amino-groups in the PEIE polymer form an interfacial dipole between ITO and active layer, which can lower the work function of the ITO and collectively act as the cathode of the solar cell. The target layer thickness of the active layer was 250 nm, similar to that in the small area control device. The 6 nm MoO_3 and then 80 nm Ag were thermally evaporated under 10^{-6} mbar base pressure. From Table 9, the power conversion
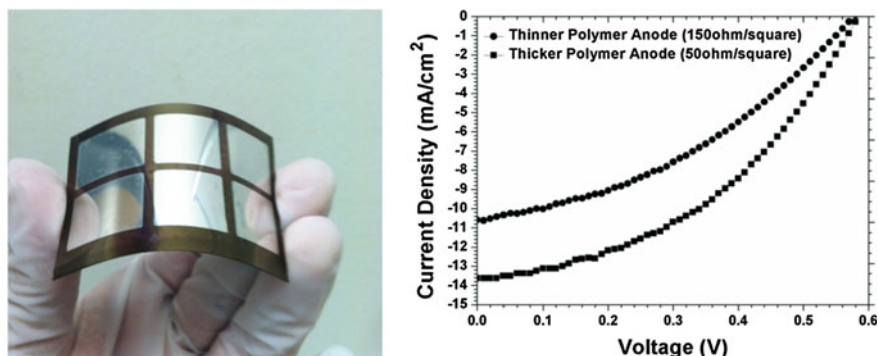
Fig. 25 The J-V characteristics of the roll-to-roll processed devices utilizing different thickness polymer anodes

Table 9 The device performances with respect to the device size which was fabricated by the roll-to-roll coating

	Jsc (A/cm^2)	Voc (V)	FF (%)	PCE (%)	Rs (Ωcm^2)	Rp (Ωcm^2)
0.00785 cm^2	11.57	0.58	53.64	3.60	8.66	468.9
4 cm^2	10.79	0.58	36.94	2.31	23.59	154.62
6 cm^2	10.66	0.58	38.94	2.41	22.87	181.56
12 cm^2	10.01	0.55	29.08	1.60	33.87	79.07

efficiency is reduced when the device size is increased. This is the result of a number of factors, including reduced fill factor, increased series resistance, and reduced shunt resistance. The blade-coated device showed better efficiency than the spin-coated device. The spin coated samples have lots of voids and aggregated particles in the polymer film as shown in Fig. 26. The shunt resistance of the spin coated device in the Table 10 is significantly reduced in device sized in 6 cm^2. This causes the lower fill factor and then lower efficiency.

2.5.4 Non-conventional Fabrication Methods Toward All-Solution Processed Polymer Solar Cells

As mentioned earlier materials such as ITO, MoO$_3$, and Ag have to be replaced with soluble materials to enable all-solution processes. Here we aim to replace the layers by polymer cathode, PEDOT:PSS and Ag nanoparticle ink, respectively, all in solution phase. To realize all-solution processable OPVs using these materials, the work function of the polymer anode should be modified with interfacial layer to create interface dipole and lower the work function [10]. Among the various materials, ammonium/amino-based organic surfactant is appropriate for the solution process such as roll-to-roll process. In addition, the PEDOT:PSS should has a
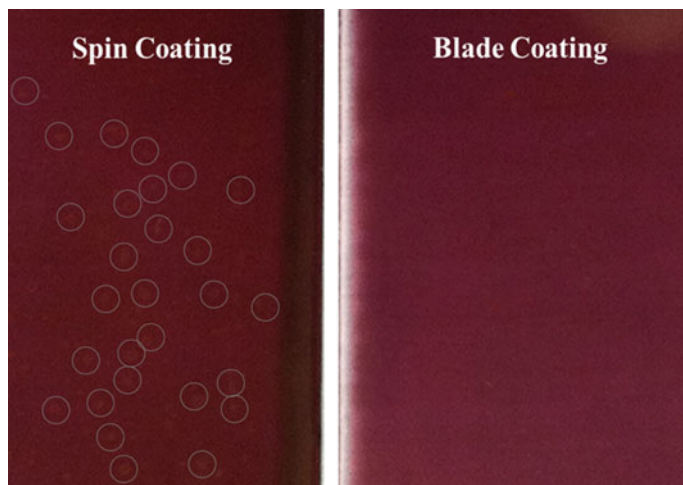
Fig. 26 The coating quality images of the blade-coated layers versus spin-coated layer. The circles indicate the voids on the P3HT:PC$_{61}$BM layer. The images were captured with X5 magnification rate

Table 10 The device performances of the blade-coated device and spin-coated device

	Jsc (A/cm^2)	Voc (V)	FF (%)	PCE (%)	Rs (Ω cm^2)	Rp (Ω cm^2)
Blade, 6 cm^2	10.66	0.58	38.94	2.41	22.87	181.56
Spin, 6 cm^2	11.21	0.50	35.27	1.98	22.17	95.06

good coat-ability on the hydrophobic polymer active layer. Moreover, the Ag nanoparticle ink should not affect the underlying layers during the coating process. Unfortunately, because the PEDOT:PSS is water-based polymer solution, it is unable to be coated on the polymer active layer. In addition, the Ag nanoparticle ink is easy to infiltrate and contaminate the underlying layer. To avoid these problems, we used nonconventional methods such as lamination or transfer technique to make the OPVs: the two layers will be coated on a separate substrate at first, and then the dried layers will be transferred to be laminated on the surface of the polymer active layer. After lamination, the contact between the two parts such as PEDOT:PSS and active polymer layer are not perfect. Thus, thermal annealing can improve the contact between the layers.

2.5.5 All-Solution Processed Lamination Technique

As a proof-of-concept experiment, the ITO-PET and ITO-glass were used to verify the feasibility of the lamination technique as an alternative process. The brief fabrication process is as follow (Fig. 27). The ZnO nanoparticle solution was
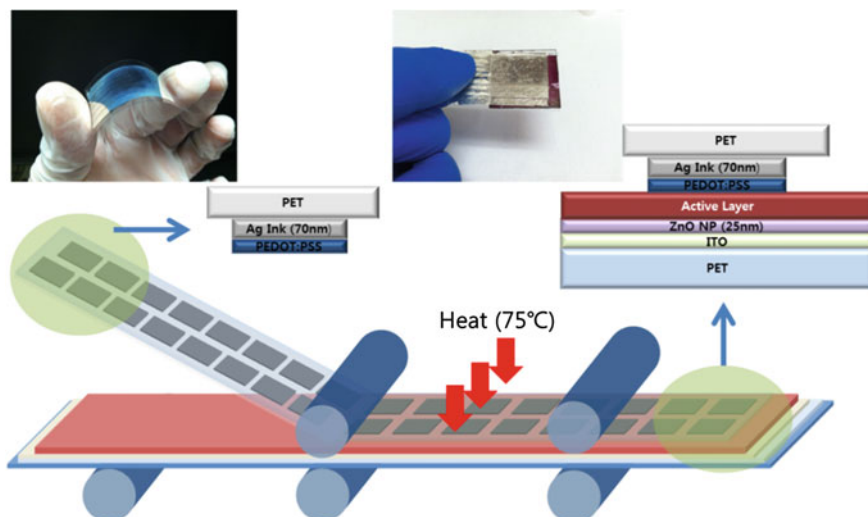
Fig. 27 Schematic diagram of the ideal lamination process and embedded images of the patterned Silver layer (*left*) and Laminated device (*right*)

spin-coated on the ITO-PET or ITO-glass. The P3HT:PC_{61}BM was spin-coated on the ZnO nanoparticle layer. On a separate PET substrate, the Ag nanoparticle ink was spin-coated, and then the PEDOT:PSS was spin-coated over the silver film. Finally, the two parts were laminated together on the hot plate at 130 °C for 5 min. The Ag electrode was patterned previously to have a role of the anode. Figure 35 shows the proposed continuous process to produce large area OPVs by using lamination technique. Because the metal film could not infiltrate through the voids or defects in the active layer, the lamination process is helpful to maintain the high shunt resistance in the large-scale devices. Moreover, the PET substrate acts as a barrier film preventing the oxygen and moisture from diffusing into the Ag layer and the active polymer layer.

The power conversion efficiency of the laminated device is 2.76 % using the ITO glass in the small area device (1 mm diameter, Fig. 28) as summarized in Table 11. The device performance of the ITO-glass is better than the ITO-PET, because the sheet resistance of the ITO-glass was 10 Ω/sq and the ITO-PET was 20 Ω/sq.

For larger device low-band gap polymer (iI-T3) was used. The ZnO nanoparticle layer and polymer active layer was blade-coated to 30 and 100 nm thickness respectively. The device performance is promising for the large area devices (2 and 3 cm^2). Generally, when the device size is increased, shunt resistance is decreased. The shunt resistance of the lamination processed device is higher than that of the evaporated device. In the large-size device, the efficiency of the optimized device was 2.27 % for 3 cm^2 devices as shown in Table 12. The series resistance was reduced after the thermal annealing (Table 14), due to improved contact at the laminated interface.

Fig. 28 The device performance of the laminated devices using ITO-glass and ITO-PET
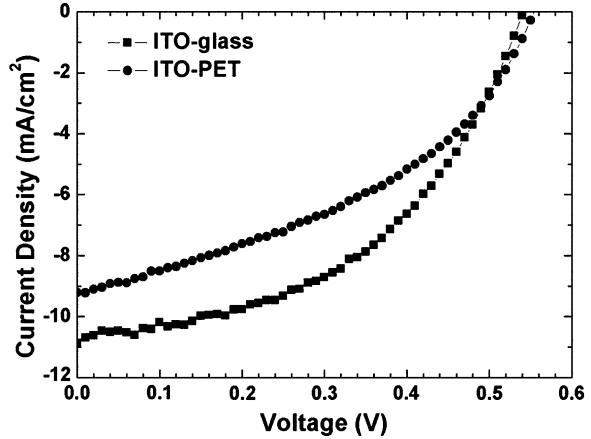

Table 11 The device performances fabricated by the lamination process

Device	Jsc (mA/cm^2)	Voc (V)	FF (%)	PCE (%)
ITO-PET	9.21	0.56	40.95	2.11
ITO-glass	10.87	0.55	46.1	2.76

2.5.6 Influence of Series Resistance in Large Area Solar Cells

We have already seen the impact of series resistance in large area device to the achievable OPV efficiency. Practical large area solar cell devices suffer more from resistive losses, which should be minimized to maintain the performance of the devices. We will quantify the effect of series resistance, R_S by computing the resistive power loss. In small area devices, organic semiconducting active layers contribute more to the resistive power loss than other factors. However, as the size of the devices increases, the R_S of the transparent electrodes become the main factor of the resistive loss [17]. The total resistive power loss per unit area is given by

$$P_R = \frac{R_S(J_{max}A)^2}{A} = R_S A J_{max}^2, \tag{15}$$

where P_R is the total resistive power loss per unit area, R_S is the series resistance in the device, J_{max} the current density, and A the area of the devices. R_S in organic solar cell contains the resistances of the anode, active layer, contacts, and cathode:

$$R_S = R_{anode} + R_{active} + R_{contacts} + R_{cathode}, \tag{16}$$

where R_{active} and $R_{contacts}$ are the series resistances of active layer and contacts of each layer, respectively. When we assume the conventional structure of organic solar cell, cathode side is the reflective metal and the anode side is the transparent

Table 12 The performances in the large-scale device fabricated by the lamination process

	Jsc (A/cm^2)	Voc (V)	FF (%)	PCE (%)	Rs (Ω cm^2)	Rp (Ω cm^2)
Non	3.62	0.73	37.59	0.99	93.26	516.62
100 °C, 5 min	6.58	0.71	44.94	1.50	34.53	506.63
100 °C, 10 min	7.04	0.69	46.71	2.27	21.59	371.70
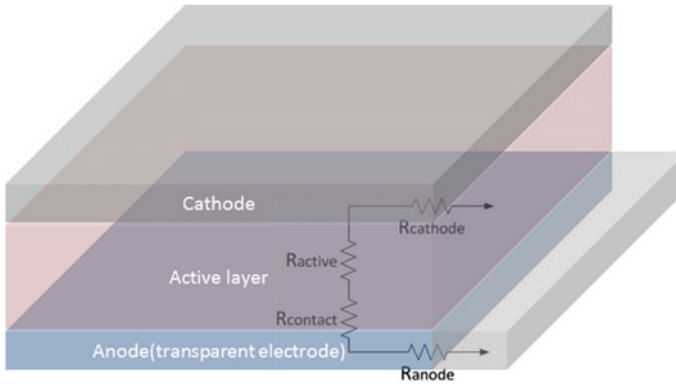
Fig. 29 Description of series resistance components inside conventional OPV cells

electrode. R_{active} and R_{contacts} does not increase with area scaling since they are vertical components in the cell which have the same carrier travel distance regardless of cell area. Furthermore, the metal cathode has negligible series resistance compared to transparent anode electrode such as ITO, with typical conductivity ratio of $\sim 100{:}1$ [18]. Therefore, the main factor that determines the resistive loss with increasing device size is the resistance of transparent electrode. Figure 29 shows each component inside the cell graphically.

The effect of the series resistance can be studied in more detail with the non-ideal equivalent circuit model, which is widely acceptable for both inorganic solar cells and organic solar cells [19]. With the parasitic resistances included, the diode equation becomes

$$J(V) = J_0 \left(e^{\frac{q(V - J(V)R_S A)}{nkT}} - 1 \right) + \frac{V - J(V)R_S A}{R_{\text{sh}} A} - J_{\text{ph}}, \qquad (17)$$

where J_0 is the reverse saturation current, V is the applied voltage, J is the current density of the cell, n is the diode ideality factor, k is Boltzmann's constant, T is temperature, R_S is series resistance, R_{sh} is shunt resistance and J_{ph} is the photo-current generated by the cell. The parameters J_0, n, R_S, R_{sh}, and J_{ph} can be obtained by fitting the diode model to the experimental J–V data from actual OPV devices under illuminated and dark conditions. Servaites et al. [20] showed the impact of R_S on the performance of large area P3HT:PCBM BHJ OPVs using ITO anode.
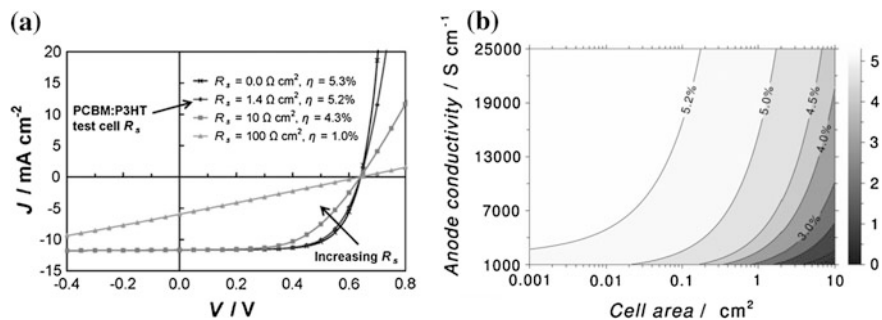
Fig. 30 **a** The effect of R_S variation on projected J–V characteristics for the P3HT:PCBM test cell. **b** The effect of anode conductivity and cell area on cell power conversion efficiency for the P3HT:PCBM test cell. Reproduced from [20] with permission of Wiley-VCH Verlag GmbH & Co. KGaA © 2010

Figure 30 shows the effect of R_S variation on the J–V curves for the P3HT:PCBM test cell. In the graph, R_S is the only parameter that changes and all the other parameters in Eq. (16) are kept constant. The results show that the resistive losses due to R_S remain negligible with cell areas under ~ 0.1 cm^2. However, as cell area increases over 0.2 cm^2, the efficiency starts to drop significantly due to steep increase of anode series resistance. Figure 30b shows the relationship between anode conductivity and cell area on power conversion efficiency of the P3HT:PCBM device, illustrating the importance of the anode conductivity as the cell size increases.

2.5.7 Design Strategy of Transparent Electrode for Low Series Resistance

To reduce the series resistance of the transparent electrode of the large area OPVs, metal grid patterns can be added to the anode side to reduce the resistive loss. Deliberate design of electrode geometry is imperative. Several strategies have been employed to reduce the negative effect of the series resistance on OPVs including bus bar design [17], ring type design [21], stripe type design [22], and deep trench type metal grating design with conductive polymer [23]. Stripe design of the large area OPVs is the most popular type due to its simplicity and adaptability to roll-to-roll process. The resistive losses from relatively high resistance of the transparent electrode can be minimized by reducing the travel distance of the photo-generated charges at the transparent electrode. The simplest way to achieve this is by putting at least one side of metal lines as close as possible to the regions of photocurrent generation. In other words, the width of the PV cell stripe should be kept narrow with the contacts put on the long sides while the length of the stripe does not matter as long as each layer of the solar cell device has no defects or discontinuities. The effects of the width of the stripe in organic solar cells were

Fig. 31 Calculated power conversion efficiency of a P3HT:PCBM-based single *rectangular* organic solar cell as a function of the width of the electrode. Two cases are shown, an ITO sheet resistance of 15 Ω/sq (*solid line*) and 60 Ω/sq (*dashed line*). Reproduced from [24] with permission from Elsevier © 2007
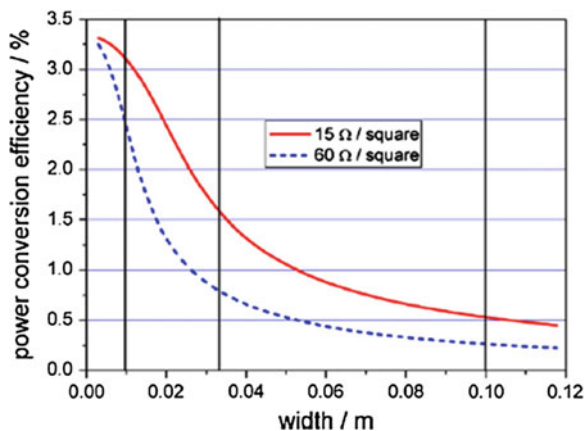
investigated by Lungenschmied et al. [24]. They calculated theoretical power conversion efficiencies of a P3HT:PCBM BHJ cells with two cases of ITO sheet resistance, 15 and 60 Ω/sq. As shown in Fig. 31, the rapid decrease of the power conversion efficiency with increasing width of the rectangular solar cell can be observed while the length of the device kept same, indicating that the performance of stripe typed large area OPV devices are mainly affected by the width of the stripes as a result of the series resistance of the transparent electrode.

Another effective way to reduce the R_S of transparent electrode is the combination of metal mesh and PEDOT:PSS to serve as transparent electrode [25]. By increasing the metal width and reducing the mesh period, the sheet resistance can be made smaller than the conventional ITO electrode. A trade-off between the optical transmittance and electrical conductivity still exists, though much smaller than that of ITO [25]. This trade-off can be further compensated by embedding high aspect-ratio metal mesh into conductive polymer, which eliminates the low optical transmittance problem without sacrificing the conductivity. Kuang et al. [23] fabricated a nanoscale metallic grating with optical transparency over 80 % and low electrical resistance under 2.4 Ω/sq. To make the structure, a polyurethane (PU) grating structure was prepared for oblique metal deposition and argon ion milling process to get the metal layers on the PU sidewalls. The typical sheet resistance of the patterned structures with gold and silver were 9.6 and 3.2 Ω/sq, respectively, which are lower than the sheet resistance of ITO for typical applications of OPVs and OLEDs.

2.5.8 Fine Metal Mesh Design for Transparent Electrode

Previously, we demonstrated normal type OPVs by using fine transparent metal mesh electrodes (TME) made by nanoimprinting [25] and transfer-printing [26] techniques. Recently, we fabricated TME by conventional photolithography
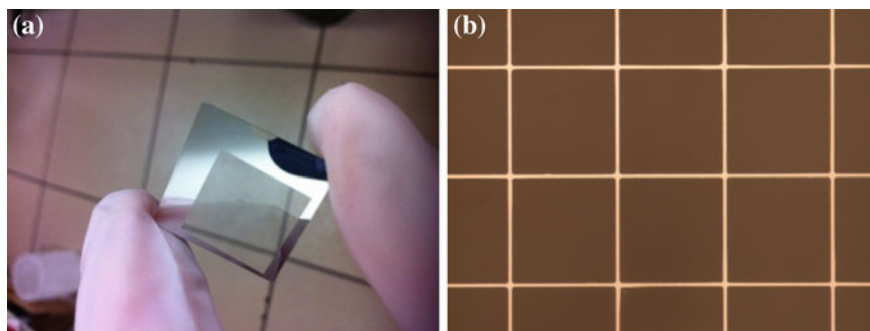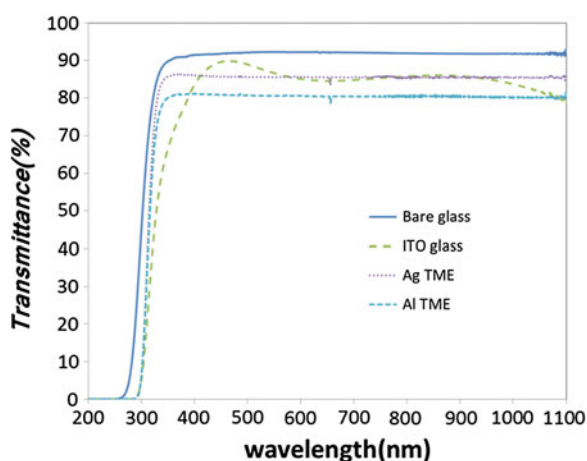
Fig. 32 **a** The fabricated transparent metal electrode on glass. **b** The optical microscope image of the fabricated transparent silver electrode. The line width of silver is 5 μm and the distance between lines is 150 μm

Fig. 33 UV–Vis transmittance spectra of bare glass, ITO glass, and the transparent Ag, Al mesh electrodes

technique and successfully fabricated inverted type OPVs with the TMEs using aluminum and silver with 150 μm cell size and 5 μm line width (Fig. 32). The thickness of the patterned TMEs for both metals was 50 nm. Figure 33 shows the UV–vis transmittance spectra from 200 to 1100 nm wavelength range of the TME. The transmittance of Ag TME substrate was 85 %, which is comparable to ITO glass. The transmittance of Al TME was 80 %, which is slightly lower than ITO glass and Ag TME substrate. Inverted solar cells were fabricated with structure shown in Fig. 34. On the TME substrates, PEDOT:PSS was spun-coated to planarize the TME patterns. Polyethylenimine ethoxylated (PEIE) solution was coated subsequently to reduce the work-function of the PEDOT:PSS for it to function as a cathode for extracting electrons [27]. Both P3HT:$PC_{61}BM$ and a low band gap polymer PIDT-phanQ:$PC_{71}BM$ [28] bulk heterojunction system were
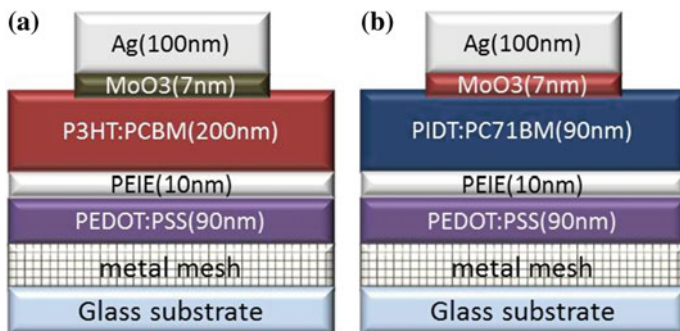
Fig. 34 The device structure of the inverted TME solar cell for **a** P3HT:CBM bulk heterojunction. **b** PIDT-phanQ:PCBM bulk heterojunction
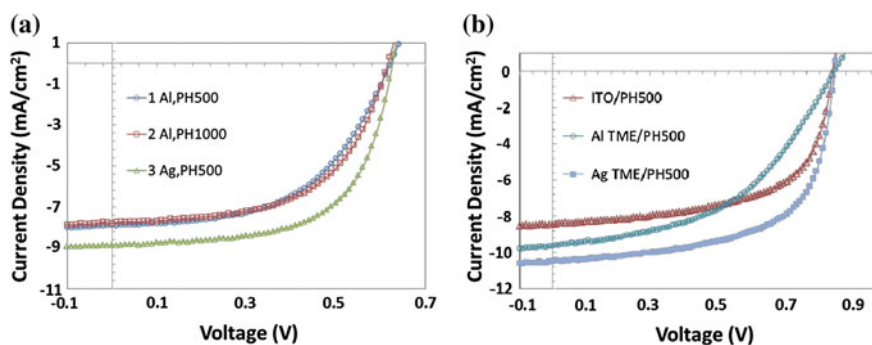

Fig. 35 J-V characteristics of organic solar cells fabricated using different transparent metal electrodes. **a** P3HT:PCBM BHJ inverted cells with Al TME/PH500, Al TME/PH1000, and Ag TME/PH500. **b** PIDT-phanQ:PC71BM BHJ inverted cells with ITO glass/PH500, Al TME/ PH500 and Ag TME/PH500

used to fabricate the solar cells. MoO_3 and silver were deposited sequentially for the anode formation.

To compare the performance of the TME substrates for organic solar cell application two PEDOT:PSS materials with different conductivity, pristine PH500 $\sigma = 0.2$ S/cm) and PH1000 ($\sigma = 0.4$ S/cm) purchased from HC Starck, were used to compare the performance of Al and Ag TME electrodes. The current density versus voltage characteristics are shown in Fig. 35. The figures of merits are summarized in Table 13. When we compare the P3HT:PC_{61}BM BHJ device with Al TME and Ag TME (Table 13), the OPV with Ag TME showed superior performance than Al TME due to the higher conductivity of Ag. In Table 14, the Ag TME-based OPV devices were compared with ITO based OPV devices for the PIDT-phanQ:PC_{71}BM BHJ system. The OPV with Ag TME showed the best performance with higher current density and fill factor compared to the OPV with

Table 13 Device characteristics of solar cells fabricated by transparent metal mesh of (a) P3HT:PCBM BHJ inverted cell

P3HT:PCBM	Jsc (mA/cm^2)	Voc (V)	FF (%)	PCE (%)	Rs (Ω cm^2)	Rsh (Ω cm^2)
Al TME/PH500	7.90	0.63	52.46	2.62	19.52	3588.17
Al TME/PH1000	8.20	0.63	56.22	2.89	11.85	767.65
Ag TME/PH500	9.01	0.64	61.57	3.53	6.29	1932.42

Table 14 Device characteristics of solar cells fabricated by transparent metal mesh of PIDT-phanQ:PC71BM BHJ inverted cell

PIDT-phanQ:PC$_{71}$BM	Jsc (mA/cm^2)	Voc (V)	FF (%)	PCE (%)	Rs (Ω cm^2)	Rsh (Ω cm^2)
ITO/PH500	8.53	0.87	59.62	4.41	5.95	1320.41
Al TME/PH500	9.66	0.88	46.90	3.99	32.10	591.74
Ag TME/PH500	10.54	0.88	61.49	5.68	4.14	1927.38

Al TME and ITO electrode. One of the reasons is that Ag TME with PH500 show the lowest R_S. Once again these results show the importance of R_S in determining the OPV overall efficiency.

3 Conclusions and Discussion

This chapter described various coating methods that can be used for large area PLED and OPVs. The coating mechanisms and instability issues in practical solution process have been examined. Using the various coating process such as roll-to-roll coating, blade coating, blade-slit coating, and spin coating, the coating performance was compared in terms of the film uniformity and controlling the coating instabilities. The blade and roll-to-roll coating are more favorable for the large-scale device in terms of the device performance and the manufacturing cost. Metal mesh structures in combination with conductive polymers was introduced as the ITO-free transparent electrode. Finally, nonconventional process such as lamination and transfer techniques was used to improve the shunt resistance and the series resistance in the large-scale and vacuum-free processed devices. However, several other issues remained to be overcome such as the lifetime stability and environmentally friendly solvents, and materials costs for the realization toward $1/W OPVs. The polymer electronics are growing fields, more research efforts are needed to improve the device performance, lifetime, process-ability, and large area manufacturing, which will bring the bright future of the polymer electronics to reality.

References

1. Tang CW (1986) Two-layer organic photovoltaic cell. Appl Phys Lett 48:183–185
2. Baldo MA, O'Brien DF, Thompson ME, Forrest SR (1999) Excitonic singlet-triplet ratio in a semiconducting organic thin film. Phys Rev B 60:14422–14428
3. Yu G, Gao J, Hummelen JC, Wudl F, Heeger AJ (1995) Polymer photovoltaic cells: enhanced efficiencies via a network of internal donor-acceptor heterojunctions. Science 270:1789–1791
4. He Z, Zhong C, Su S, Xu M, Wu H, Cao Y (2012) Enhanced power-conversion efficiency in polymer solar cells using an inverted device structure. Nat Photon 6:591–595
5. Espinosa N, García-Valverdea R, Krebs FC (2011) Life-cycle analysis of product integrated polymer solar cells. Energy Environ Sci 4:1547–1557
6. Hall DB, Underhill P, Torkelson JM (1998) Spin coating of thin and ultrathin polymer films. Polym Eng Sci 38:2040–2045
7. Weinstein SJ, Ruschak KJ (2004) Coating flows. Annu Rev Fluid Mech 36:29–53
8. Landau L, Levich B (1942) Dragging of a liquid by a moving plate. Acta Physicochim URSS 17:42–54
9. Stalder R, Grand C, Subbiah J, So F, Reynolds JR (2012) An isoindigo and dithieno [3,2-b:2′,3′-d]silole copolymer for polymer solar cells. Polym Chem 3:89–92
10. Youn H, Yang M (2010) Solution-processed polymer light-emitting diodes utilizing a ZnO/organic ionic interlayer with Al cathode. Appl Phys Lett 97:243302
11. Yu Z, Zhang Q, Chen LLQ, Niu X, Liu J, Pei Q (2011) Highly flexible silver nanowire electrodes for shape-memory polymer light-emitting diodes. Adv Mater 23:664–668
12. Han T-H, Lee Y, Choi M-R, Woo S-H, Bae S-H, Hong BH, Ahn J-H, Lee T-W (2011) Extremely efficient flexible organic light-emitting diodes with modified graphene anode. Nat Photon 6:105–110
13. Li J, Hu L, Wang L, Zhou Y, Grüner G, Marks TJ (2006) Nano Lett 6:2472–2477
14. Lee BH, Park SH, Back H, Lee K (2011) Novel film-casting method for high-performance flexible polymer electrodes. Adv Mater 21:287–493
15. Shin S, Yang M, Guo LJ, Youn H (2013) Noble roll-to-roll cohesive, coated, flexible, high-efficiency polymer light-emitting diodes utilizing ITO-free polymer anodes. Small 9:1–9
16. Youn H, Jeon K, Shin S, Yang M (2012) All-solution blade-slit coated polymer light-emitting diodes. Org Electron 13:1470–1478
17. Choi S, Potscavage WJ, Kippelen B (2009) Area-scaling of organic solar cells. J Appl Phys 106:054507
18. Yang Y, Jin S, Medvedeva JE, Ireland JR, Metz AW, Ni J, Hersam MC, Freeman AJ, Marks TJ (2006) CdO as the archetypical transparent conducting oxide. Systematics of dopant ionic radius and electronic structure effects on charge transport and band structure. JACS 127:8796–8804
19. Cheknane A, Hilal HS, Djeffal F, Benyoucef B, Charles J-P (2008) An equivalent circuit approach to organic solar cell modelling. Microelectron J 39:1173–1180
20. Servaites JD, Yeganeh S, Marks TJ, Ratner MA (2010) Efficiency Enhancement in organic photovoltaic cells: consequences of optimizing series resistance. Adv Funct Mater 20:97–104
21. Krebs FC, Jørgensen M, Norrman K, Hagemann O, Alstrup J, Nielsen TD, Fyenbo J, Larsen K, Kristensen J (2009) A complete process for production of flexible large area polymer solar cells entirely using screen printing—first public demonstration. Sol Energy Mater Sol Cells 93:422–441
22. Angmo D, Hösel M, Krebs FC (2012) All solution processing of ITO-free organic solar cell modules directly on barrier foil. Sol Energy Mater Sol Cells 107:329–336
23. Kuang P, Park J-M, Leung W, Mahadevapuram RC, Nalwa KS, Kim T-G, Chaudhary S, Ho K-M, Constant K (2011) A new architecture for transparent electrodes: relieving the trade-off between electrical conductivity and optical transmittance. Adv Mater 23:2469–2473

24. Lungenschmied C, Dennler G, Neugebauer H, Sariciftci SN, Glatthaar M, Meyer T, Meyer A (2007) Flexible, long-lived, large-area, organic solar cells. Sol Energy Mater Sol Cells 91:379–384
25. Kang M-G, Kim M-S, Kim J, Guo LJ (2008) Organic solar cells using nanoimprinted transparent metal electrodes. Adv Mater 20:4408–4413
26. Kang M-G, Park HJ, Ahn S-H, Guo LJ (2010) Transparent Cu nanowire mesh electrode on a flexible substrate fabricated by simple transfer printing and its application in organic solar cell. Sol Energy Mater Sol Cells 94:1179–1184
27. Zhou Y, Fuentes-Hernandez C, Shim J, Meyer J, Giordano AJ, Li H, Winget P et al (2012) A universal method to produce low–work function electrodes for organic electronics. Science 336:327–332
28. Zhang Y, Zou J, Yip H-L, Chen K-S, Zeigler DF, Sun Y, Jen AK-Y (2011) Indacenodithiophene and quinoxaline-based conjugated polymers for highly efficient polymer solar cells. Chem Mater 23:2289–2291